ACES Asian Chemical Editorial Society

doi.org/10.1002/cnma.202400459

CHEMNANOMAT
Research Article

www.chemnanomat.org

Tightly Interfaced Cu_2O with In_2O_3 to Promote Hydrogen Evolution in Presence of Biomass-Derived Alcohols

Salvatore Impemba,[a, b] Giacomo Provinciali,[a] Jonathan Filippi,[a] Stefano Caporali,[c] Beatrice Muzzi,[a] Andrea Casini,[b] and Maria Caporali*[a]

By a mild and straightforward synthetic protocol in aqueous solution and without surfactants, hierarchical Cu_2O nanospheres were grown on preformed In_2O_3 nanostructures, varying the ratio In:Cu (2.5, 0.5). Accordingly, two different binary compounds In_2O_3-Cu_2O were prepared and afterwards they were integrated with TiO_2 NPs. The ternary composites having a loading of 2.0, 5.0 and 10.0 wt.% respectively of binary In_2O_3-Cu_2O, were tested as photocatalysts in the solar-driven production of hydrogen from water, using as sacrificial agents alcohols derived from the biomass. Satisfyingly, the rate of H_2 evolution (20.5 mmol/g h) resulted two orders of magnitude higher respect to bare TiO_2 (0.2 mmol/g h). Electrochemical impedance spectroscopy and photoluminescence measurements revealed the formation of a tight heterojunction between In_2O_3 and Cu_2O, which is responsible for the improved charge carrier density and transfer and for the diminished electron-hole recombination.

1. Introduction

Heterogeneous photocatalysis is one of the most important tool to face a series of different reactions, ranging from oxidations of organic molecules to hydrogen production (H_2).[1–3] Water-splitting reaction through solar technology has attracted much of the scientific community's attention as it allows to obtain H_2, a promising energy vector,[4,5] in an eco-friendly manner.[6,7] For this reason, one of the aims of scientific research is the development of increasingly active photocatalysts and recently a large number of different photoactive materials have been designed and applied in the production of solar fuels.[8–11] Greater attention is paid to those semiconductors that are constituted by elements largely available, non-toxic and chemically stable. Suitable band gap, efficient electron/hole separation and high charge transfer are key-parameters in a semiconductor that are mandatory for an efficient use of solar energy. These are influenced by physical and chemical properties such as material morphology, electronic structure, crystallinity, exposed crystal surface and material defects, and can be improved by the construction of heterojunctions.[12,13] Titanium dioxide (TiO_2) remains one of the most studied semiconductors for photocatalytic applications due to its nontoxicity, large availability, chemical stability in water, acid and base environment and resistance to photocorrosion.[14] However, due to its large band gap, it can only absorb in the UV region and for this reason, other semiconductors have been investigated to improve the solar energy utilization, such as MoS_2,[15,16] In_2S_3,[17] $ZnIn_2S_4$,[18] CdS,[19] g.C_3N_4.[20] Very interesting is indium oxide (In_2O_3), an n-type semiconductor (whose direct and indirect band gap values are 2.8 eV and 3.2 eV respectively) which, due to its chemico-physical, electrical and optical properties, has potential applications in different fields, such as photocatalysis,[21] gas sensors[22] and solar cells.[23,24] Varieties of In_2O_3-based nanocomposites have been studied showing an improvement of photocatalytic activity in several processes.[25–34] Cuprous oxide (Cu_2O) is a p-type semiconductor having a narrow band gap (2.0–2.6 eV) and a high optical absorption coefficient, that make it an excellent candidate for solar energy conversion applications.[35] It is often paired to inorganic oxide semiconductors to extend the absorption in the visible region; in this work we have studied the growth of Cu_2O NPs on In_2O_3 aiming to build a p-n heterojunction in a Type II configuration to improve the efficiency of charge transport and to reduce the tendency to photocorrosion of Cu_2O. A vast literature has been devoted to the shape-controlled synthesis of Cu_2O micro- and nanocrystals,[36] that can be summarised in two main routes: i) the use of Cu^{2+} salt as reagent in presence of a surfactant (SDS, PVP or cetyltrimethylammonium) and a reducing agent (hydroxylamine, ascorbic acid, hydrazine) or ii) pH controlled hydrolysis of copper (I) chloride (CuCl). Our procedure used copper (II) chloride ($CuCl_2$) as reagent that was mildly reduced in water at RT in the presence of preformed In_2O_3 nanostructures, without using an organic ligand as template. The resulting binary In_2O_3-Cu_2O was self-assembled with TiO_2 via ultrasonication giving a

[a] S. Impemba, G. Provinciali, J. Filippi, B. Muzzi, M. Caporali
National Research Council-Institute of Chemistry of Organometallic Compounds CNR-ICCOM, Via Madonna del Piano 10, 50019 Sesto Fiorentino, Italy
E-mail: maria.caporali@iccom.cnr.it

[b] S. Impemba, A. Casini
Department of Chemistry, University of Salerno, Via Giovanni Paolo II 132, 84084 Fisciano, Italy

[c] S. Caporali
Department of Industrial Engineering, University of Florence, Via di S. Marta 3, 50139 Firenze, Italy

Supporting information for this article is available on the WWW under https://doi.org/10.1002/cnma.202400459

series of TiO_2/In_2O_3-Cu_2O nanocomposites, having different wt% of the co-catalyst In_2O_3-Cu_2O and varying In:Cu ratio.

Experimental Section

Materials and Chemicals

TiO_2 P25 was obtained from Degussa, Indium(III) chloride hydrate ($InCl_3$·$4H_2O$, 99.99%), urea (99%), hydrazine (N_2H_4·H_2O - 98% in water) were purchased from Merck. All reagents were used without further purification.

Synthesis of In_2O_3

$InCl_3$·$4H_2O$ (146.6 mg, 0.5 mmol) and urea (120.1 mg, 2.0 mmol) were dissolved by stirring for 30 minutes in 40 ml of distilled and degassed water, for a final concentration of 0.012 M. The solution was transferred into a Teflon-lined autoclave (volume of 50 ml) and heated at 140 °C in an oven, for 16 hours. Then, the autoclave was cooled at room temperature *and the white solid product was isolated by centrifugation.* Six washing/centrifugation cycles (8000 rpm for 20 minutes) were carried out, four using distilled water and two using ethanol. The white solid of $In(OH)_3$ was collected and dried under vacuum for 6 hours. Its chemical identity and purity was assessed by XRD, see Figure S1. Afterwards, it was annealed at 600 °C for 2 hours in argon flow with a heating rate of 10 °C/min, obtaining a pale yellow powder. Yield (respect to starting $InCl_3$): 58%.

Synthesis of In_2O_3-Cu_2O with Different In:Cu Ratio

In_2O_3 previously synthetized (23.0 mg, 0.08 mmol) and $CuCl_2$ (23.5 mg, 0.17 mmol) were dispersed in 16 mL of distilled and degassed H_2O (Solution A) and ultrasonicated for 10 minutes. Afterwards, N_2H_4·H_2O (hydrazine, 26.0 mg, 0.52 mmol, 3 equiv) was dissolved in 16 mL of distilled and degassed H_2O (Solution B). Then, Solution B was added into Solution A under stirring, an orange final suspension was obtained. The latter was stirred at 900 rpm for 2 hours at room temperature, then the orange powder of In_2O_3-Cu_2O was isolated by centrifugation. Three washing/centrifugation cycles were carried out, two using distilled and degassed H_2O and one using degassed acetone, then the solid was dried under vacuum overnight to isolate the binary In_2O_3-Cu_2O (70:30). The synthesis was carried out as well using 5.10 mg of In_2O_3, leaving the rest unaltered, to obtain the binary composite In_2O_3-Cu_2O (30:70).

Pure Cu_2O NPs were synthetized following the same procedure, without using In_2O_3.

Synthesis of the Ternary Heterostructures TiO_2/In_2O_3-Cu_2O

In_2O_3-Cu_2O (ratio 70:30, 1.5 mg) previously synthetized and TiO_2 P25 (28.5 mg) were ultrasonicated for 3 hours in 20 ml of isopropanol. Then the pale orange powder of TiO_2/In_2O_3-Cu_2O was isolated by centrifugation, after adding 10 ml of degassed ethanol before the washing/centrifugation cycle. Ultimately, the solid was dried under vacuum overnight to obtain the ternary TiO_2/In_2O_3-Cu_2O 5 wt%. Following the same way, the other ternary compound having 5 wt% of In_2O_3-Cu_2O (30:70) was prepared. The final content of In and Cu was determined by ICP analysis, see Table S1.

In the case of In_2O_3-Cu_2O (70:30), the ternary composites having 2.0 and 10.0 wt% of the binary compound were also prepared.

Characterization of Samples

The morphological and compositional analysis of the samples was conducted using an SEM-EDX instrument setup. Elemental composition assessment was performed through EDX analysis, employing

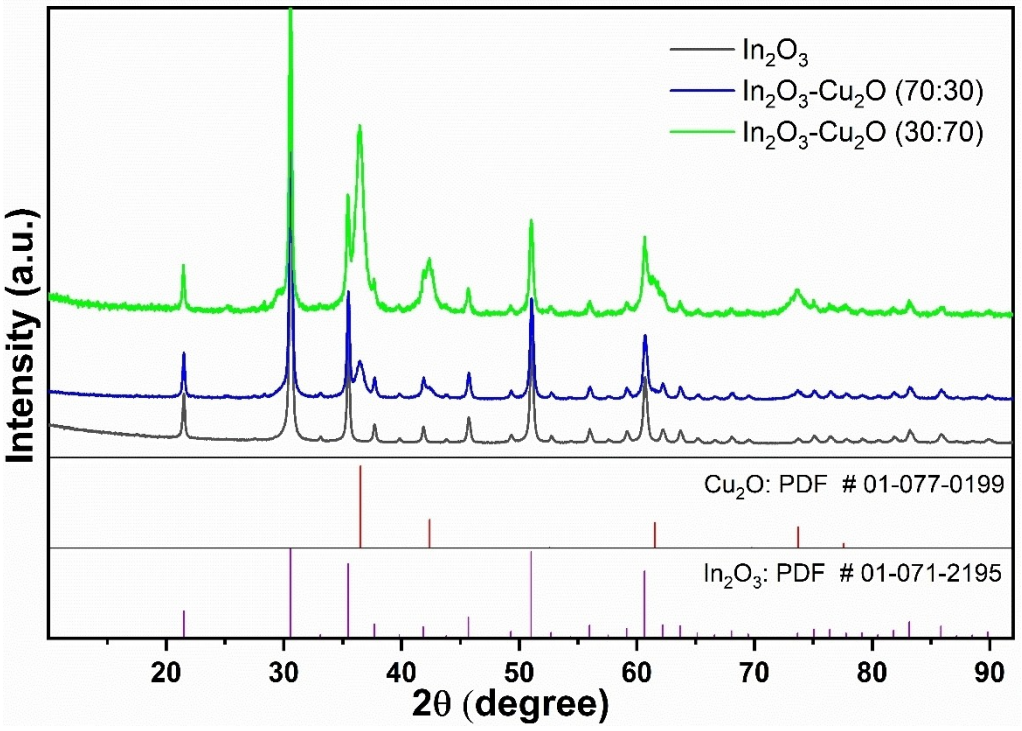

Figure 1. Comparison of PXRD of pristine In_2O_3 and its binary composites In_2O_3-Cu_2O.

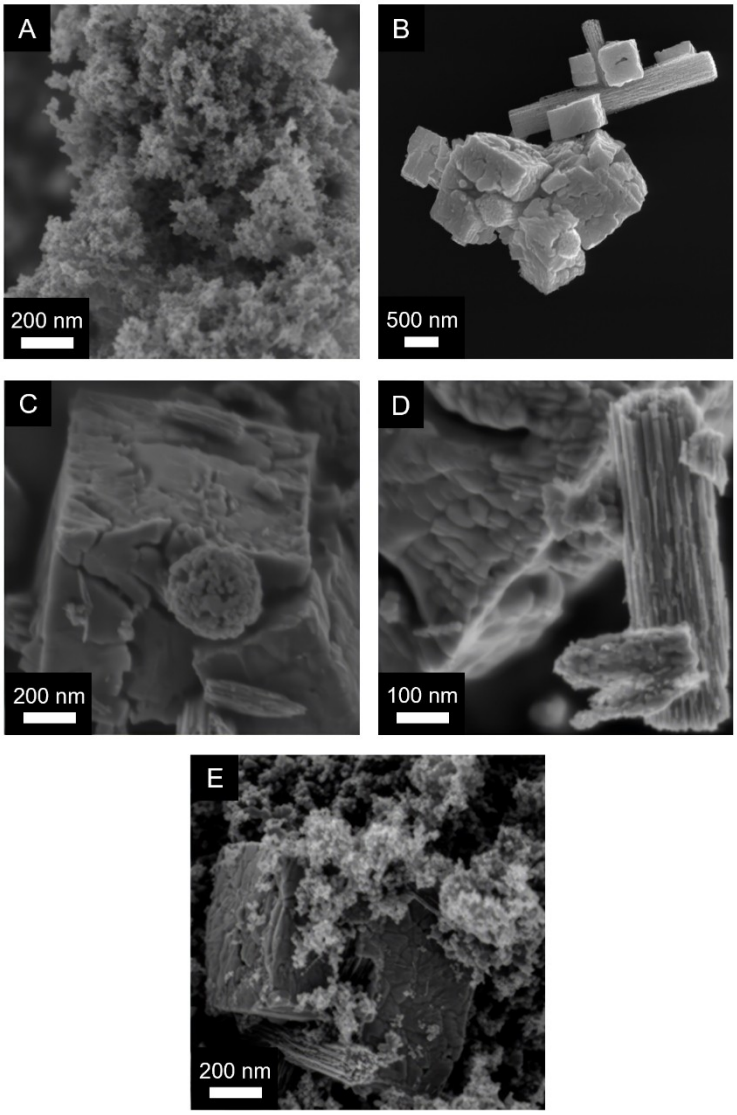

Figure 2. SEM analysis of a) pristine TiO_2; b) pristine In_2O_3; c) In_2O_3-Cu_2O (70:30) (focus on nanocubes); d) In_2O_3-Cu_2O (70:30) (focus on nanorods); e) TiO_2/In_2O_3-Cu_2O (70:30).

a silicon-drift detector interfaced with a Scanning Electron Microscope (SEM) operating at a working distance of 8.5 mm and an accelerating voltage of 10 kV. SEM micrographs of the materials were obtained using the Field Emission Gun-Scanning Electron Microscope (FEG-SEM) from Carl Zeiss Microscopy GmbH, Germany, with the settings adjusted to an acceleration voltage of 3 kV and a working distance of 3.9 mm. Following this, SEM images were processed using ImageJ's MorphoLibJ "distance transform watershed" method.[37,38] The images were converted to 8-bit and binarized, with an average threshold automatically determined.[39] Cross-correlation analysis, facilitated by a plugin developed by Chiga et al., was used to compare binarized images with their grayscale originals.[40] The image with the highest correlation and determination (R^2) coefficients was selected for further analysis. To ensure a comprehensive assessment and minimize the impact of particle aggregates, at least six regions from each SEM image were selected for binarization and detailed examination. The MorphoLibJ technique was used to isolate individual objects, and their dimensions were recorded. To confirm the reproducibility of the results, three different SEM images were analyzed for each formulation.

The High-Resolution Transmission Electron Microscopy (HR-TEM) and High-Angle Annular Dark Field Scanning Transmission Electron Microscopy (HAADF-STEM) measurements were carried out with a TALOS F200X G2 (Thermo-Fisher Scientific) equipped with a high-brightness Field Emission Gun (X-FEG, 80–200 keV), and with 4 in-column SDD Super-X detectors for energy dispersive X-ray spectroscopy (EDXS).

To determine the crystallinity and purity of the synthesized catalyst, X-ray diffraction (XRD) (Panalytical Advance X-ray powder diffractometer) was performed.

X-ray Photoelectron Spectroscopy (XPS) measurements were performed at the Chemistry Department, University of Florence (Italy) in an ultra-high vacuum (10^{-9} mbar) system equipped with a VSW HAC 5000 hemispherical electron energy analyzer and a non-monochromatized Mg–Kα X-ray source (1253.6 eV). The source power used was 100 W (10 kV×10 mA) and the spectra were acquired in the constant-pass-energy mode at E_{pas} = 44 eV. The overall energy resolution was 1.2 eV as a full-width at half maximum (FWHM) for the Ag $3d_{5/2}$ line of a pure silver reference.

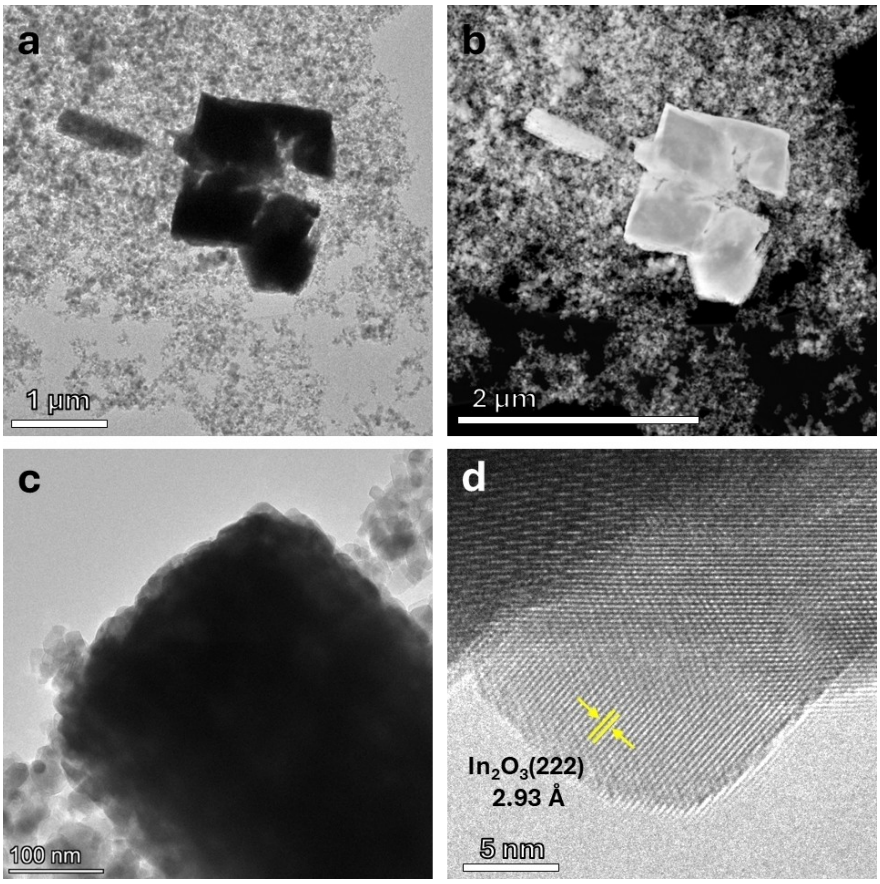

Figure 3. a) Transmission Electron Microscopy (TEM) and b) High-Angle Annular Dark Field (HAADF) images of TiO_2/In_2O_3-Cu_2O (70:30) composite. c) Enlargement of In_2O_3-Cu_2O heterostructure and d) the High-Resolution TEM image of In_2O_3.

The recorded spectra were fitted using XPS Peak 4.1 software employing Gauss-Lorentz curves after subtraction of a Shirley-type background. The samples were dropcasted from a suspension in methanol, dried under a stream of nitrogen and introduced in the UHV system via a loadlock under inert gas (N_2) flux, in order to minimize the exposure to air contaminants and kept in the introduction chamber for at least 12 hours before the measurements.

The diffuse reflectance spectra were measured by a Shimadzu UV-2600 spectrometer on the solid samples using an integrating sphere with $BaSO_4$ as a reference material. By using the Kubelka-Munk equation, Tauc plots were obtained and the optical band-gap energy of the samples was extrapolated.

Photoluminescence spectroscopy (PL) was registered using a Jasco spectrofluorometer model FP-8300. The powder samples were analysed by irradiating at a wavelength close to the maximum absorption in the corresponding UV-Vis spectrum, i.e. $\lambda = 325$ nm.

Electrochemical measurements including electrochemical impedance spectroscopy (EIS) and electrochemical response (cyclic voltammetry, CV) were carried out in a standard three electrode cell using an electrochemical workstation (PARSTAT 2273 potentiostat/galvanostat). The EIS (perturbation voltage 20 mV, frequency 100 KHz – 100 mHz) and CV were measured using a saturated Ag|AgCl|KCl reference electrode, a platinum coiled wire as the counter electrode and 0.5 M Na_2SO_4 aqueous solution as electrolyte. To prepare the working electrode, pristine TiO_2 and the synthesized samples In_2O_3, Cu_2O, and the ternary nanocomposites TiO_2/In_2O_3-Cu_2O were first dispersed in acetone (1.0 mL). The dispersion containing the catalyst (3.0 mg/mL) was deposited by drop-coating on a fluorine-doped tin oxide (FTO) conductive glass substrate (2.0 cm^2) and was dried under a stream of nitrogen before measurements. Mott-Schottky (M–S) curves were measured under an AC amplitude of 10 mV and frequency of 1 kHz.

Photocatalytic Performance Tests

The evolution of hydrogen from water was carried out in a 12 mL cylindrical quartz tube closed with a rubber cap having a silicone septum under the irradiation of a 300 W Xe lamp (Newport, USA), see Figure S1 for the image of the photocatalytic equipment. The photocatalyst (1.3 mg) was dispersed in 2.4 mL of degassed MilliQ water and 0.6 ml of degassed methanol (20 vol%) by 10 minutes ultrasonication. Then, the irradiation was started covering the full solar spectrum (UV-Vis-IR) and the system was kept to react under stirring at room temperature ($T = 25\,^{\circ}C$) for the required time. Every hour, the gases were sampled via a syringe and injected into a Shimadzu GC-2010 gas chromatograph equipped with an MS-5 A column and a thermal conductivity detector using a temperature ramp program starting from 140 °C for 9 minutes and rising to 225 °C in 25 minutes, hydrogen retention time is 3.35 min.

Results and Discussion

Cu_2O nanoparticles were grown on In_2O_3 nanostructures by a wet chemical route using variable amount of preformed In_2O_3

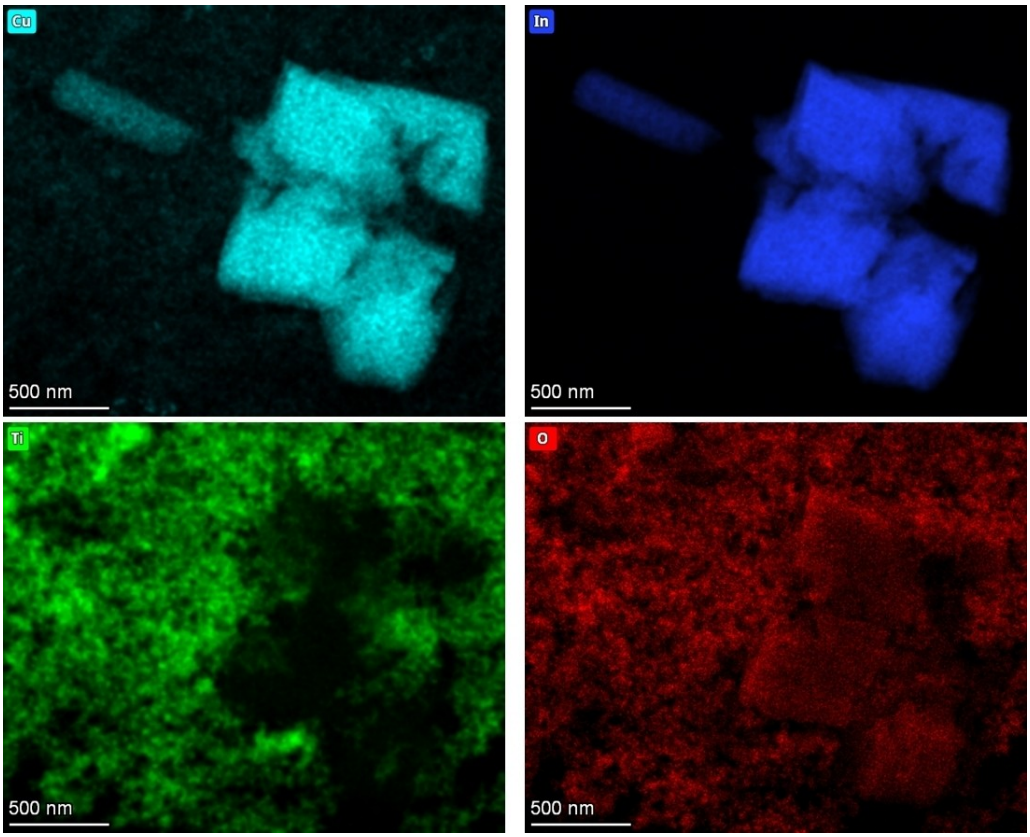

Figure 4. STEM-EDX elements (Cu, In, Ti, O) mapping distribution for the chemical composition analysis of Ti_2O/In_2O_3-Cu_2O composite.

nanostructures to get binary composites In_2O_3-Cu_2O with different In: Cu ratio 70:30 and 30:70 as described in the Experimental Section. The chemical identity and purity of the nanocomposites were ascertained by PXRD diffraction as shown in Figure 1 below, where there is a comparison of XRD spectra of pristine In_2O_3 and its binary composites In_2O_3-Cu_2O having different weight ratio.

The reflections observed for In_2O_3 at $2\theta = 21.5°$, 30.5°, 35.4°, 51.0°, 60.6° are assigned at (211), (222), (400), (440) and (622) crystallographic planes respectively. The highest intensity of the (222) diffraction peak clearly shows that the In_2O_3 is present with a cubic phase whose structural symmetry is governed by the *I*a3 space group (ICDD #98-000-6517).[41] The precursor $In(OH)_3$ was also characterized by XRD and showed peaks at $2\theta = 22.3°$ (200), 31.7° (220), 35.7° (013), 39.1° (222), 45.4° (400), 51.2° (420), 56.9° (422), 66.3° (440), 70.9° (442), 75.4° (620) and 79.9° (622) as shown in Figure S1, which agrees well with the cubic phase,[42] possessing a space group symmetry of Im3 (ICDD #98-001-7283).

The diffraction peaks of Cu_2O in the binary composites are found at $2\theta = 29.5°$, 36.4°, 42.3°, 61.3°, and 73.5° and can be safely assigned at (110), (111), (200), (220) and (311) crystallographic planes respectively. The strong peak at 36.4° indexed to the (111) plane shows that the preferred crystal orientation of Cu_2O is cubic;[43] furthermore, the signal intensity of Cu_2O is increasing sharply going from 70:30 to 30:70 binary composite, confirming in the latter a greater quantity of Cu_2O. There are no diffraction peaks attributable to impurities of CuO and/or Cu, therefore the experimental procedure affords crystalline and pure Cu_2O NPs grown on In_2O_3.

Afterwards, the binary derivatives were integrated with TiO_2 nanoparticles by self-assembly under ultrasonication, yielding the corresponding ternary nanocomposites TiO_2/In_2O_3-Cu_2O with different In:Cu ratio. The Figure S2 shows the PXRD spectrum of the ternary heterostructure TiO_2/In_2O_3-Cu_2O having 70:30 weight ratio. The diffraction peaks of anatase TiO_2[44] appeared at $2\theta = 25.3°$ (011), 37.7° (004), 48.0° (020), 62.7° (024) and 75.0° (125) while those of rutile TiO_2[45] were observed at $2\theta = 27.4°$ (110), 41.2° (111), 54.3° (121), 69.0° (031), and 69.8° (112). The diffraction peaks of In_2O_3 and Cu_2O were present confirming the composite was successfully prepared.

SEM images of the binary In_2O_3-Cu_2O (70:30) and of the corresponding ternary composite TiO_2/In_2O_3-Cu_2O (70:30) are collected in Figure 2, together with a reference image of spherical TiO_2 NPs (Figure 2a) which are sized in the 10–50 nm diameter range and an overview of pristine In_2O_3 nanostructures (Figure 2b).

The two binary composites In_2O_3-Cu_2O are constituted by Cu_2O NPs well dispersed on the surface of In_2O_3 nanostructures. Careful SEM inspection revealed hierarchical nature for Cu_2O particles, comprising smaller nanoparticles with average diameter $D_n = 25$ nm, that aggregate into larger spherical structures having an average diameter $D_m = 365$ nm (Figure S4 panel A_1, B_1) in the case In_2O_3-Cu_2O (70:30). Meanwhile for the other

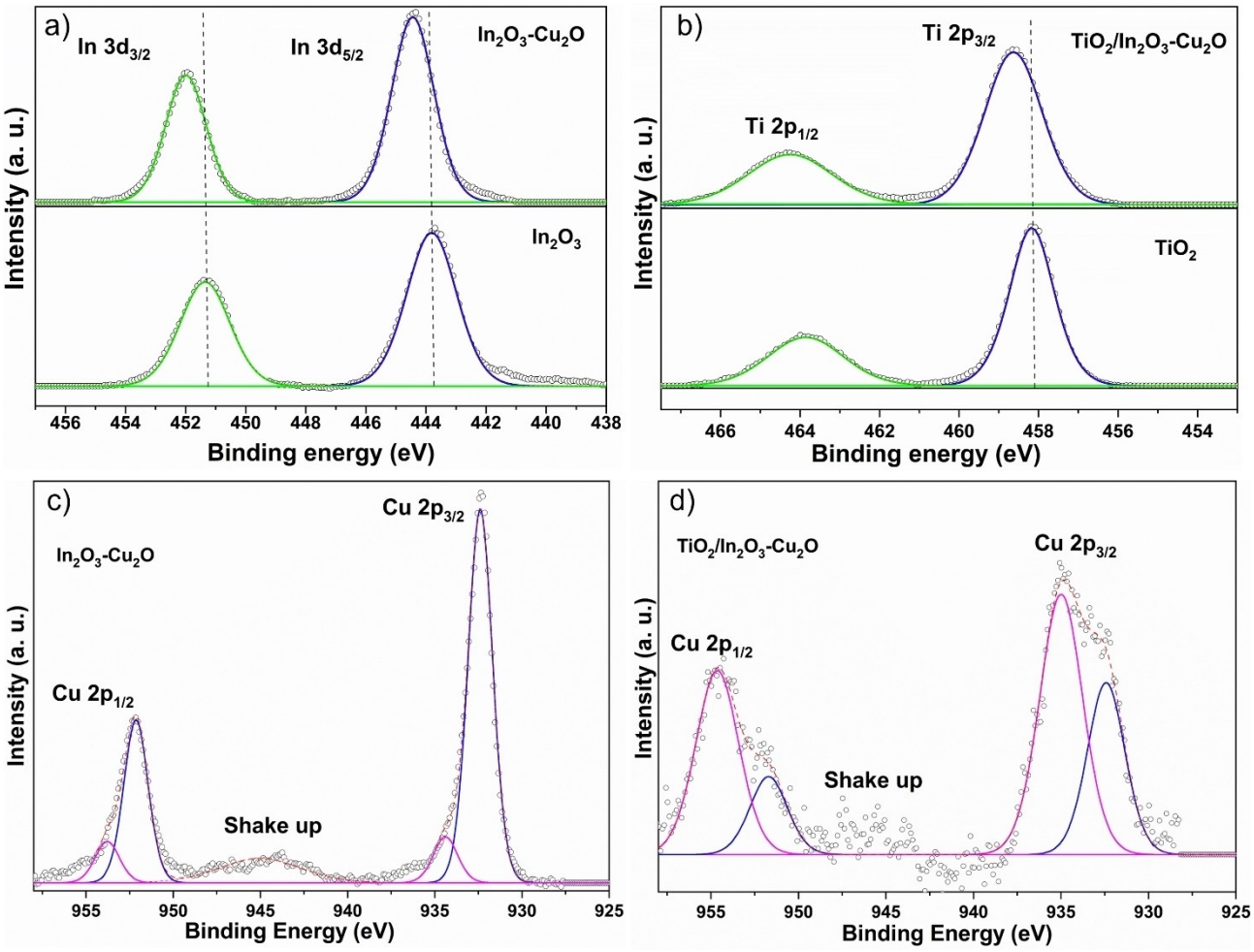

Figure 5. a) XPS core level of In 3d; b) XPS core level of Ti 2p; c) and d) XPS core level of Cu 2p.

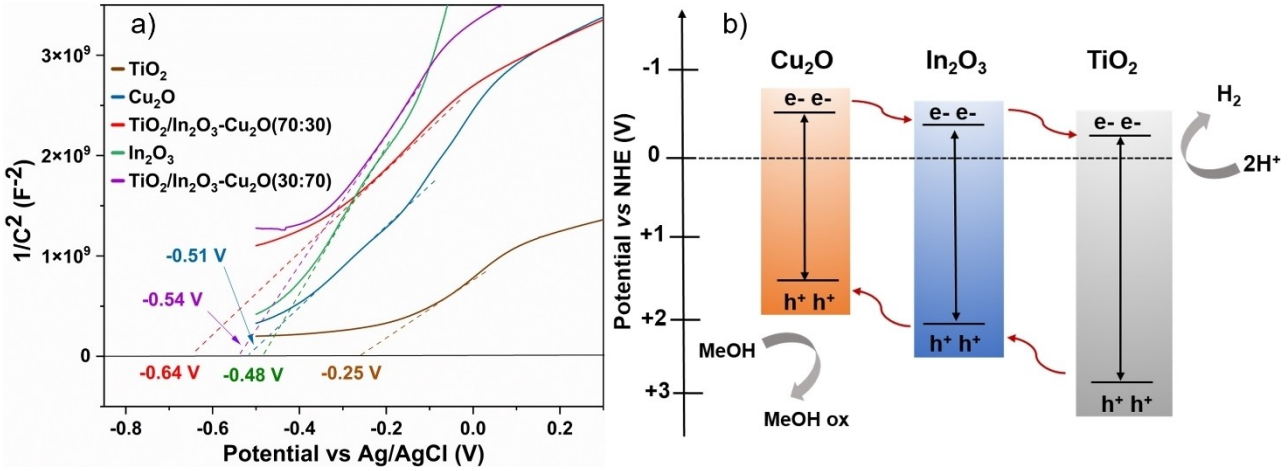

Figure 9. a) Mott-Schottky plots of pristine TiO_2, In_2O_3, Cu_2O, the binary In_2O_3-Cu_2O and the ternary TiO_2/In_2O_3-Cu_2O. Dashed lines show an approximate linear fit used to estimate the V_{fb}; b) Band structure alignment for TiO_2, In_2O_3 and Cu_2O.

binary compound (30:70) the average size is smaller and centered around 300 nm (Figure S4 panel A_2, B_2). Regarding In_2O_3 nanostructures, SEM analysis highlights the presence of In_2O_3 nanocubes (Figure 2b,c) having an average side dimension of approximately 900 nm (Figure S5) and In_2O_3 nanorods (Figure 2b–d) that show as well a hierarchical structure, with an average length of about 1.3 μm, formed by the assembly of

individual nanorods (Figure S6). The corresponding size distributions are reported in Figure S7–S8–S9.

The SEM image of the ternary composite TiO_2/In_2O_3-Cu_2O (70:30) revealed In_2O_3 and Cu_2O nanostructures buried beneath TiO_2 nanoparticles being the latter the major component of the composite (Figure 2e) as confirmed by SEM-EDX mapping (Figure S10). SEM image of the other ternary composite TiO_2/In_2O_3-Cu_2O (30:70) is shown in Figure S3.

TEM and HAADF-STEM images (Figures 3a and b, respectively), are shown as representative of the whole sample and display micrometric cube/rod surrounded by TiO_2 NPs with average size around 25 nm as observed by SEM, see Figure 2a. To establish the crystal structure of the micrometric systems, HR-TEM images were acquired (Figure 3d). These images showed the lattice fringes spacing of 2.93 Å, characteristic of the (222) planes of In_2O_3 phase (space group)$Ia\bar{3}$. To assess the presence of Cu_2O NPs on In_2O_3 structures, STEM-EDX elements mapping distribution were recorded (Figure 4). The STEM-EDX maps of Cu, In, Ti and O demonstrated a uniform distribution of Cu_2O on In_2O_3 structures, which validate the formation of a binary system In_2O_3-Cu_2O with a surprisingly extended contact interface.

To evaluate the oxidation state of the elements in the nanocomposites, XPS was performed both for binary and ternary derivatives. Concerning XPS of In 3d, the spectrum observed for the binary compound In_2O_3-Cu_2O (70:30) contains two characteristic peaks at B.E. = 444.4 eV and B.E. = 451.9 eV (see Figure 5a) corresponding to In $3d_{5/2}$ and In $3d_{3/2}$ respectively, which result shifted to higher binding energy of $\Delta = +0.6$ eV respect to pristine In_2O_3, having peaks at B.E. = 443.8 eV and B.E. = 451.3 eV (Figure 5a). For the corresponding ternary derivative TiO_2/In_2O_3-Cu_2O (70:30), being the content of In_2O_3 under the threshold sensitivity of the instrument, the In 3d peaks could not be detected, meanwhile the core level XPS spectrum of Ti 2p was measured and compared with pristine TiO_2. As shown in Figure 5b, for bare TiO_2 two peaks were

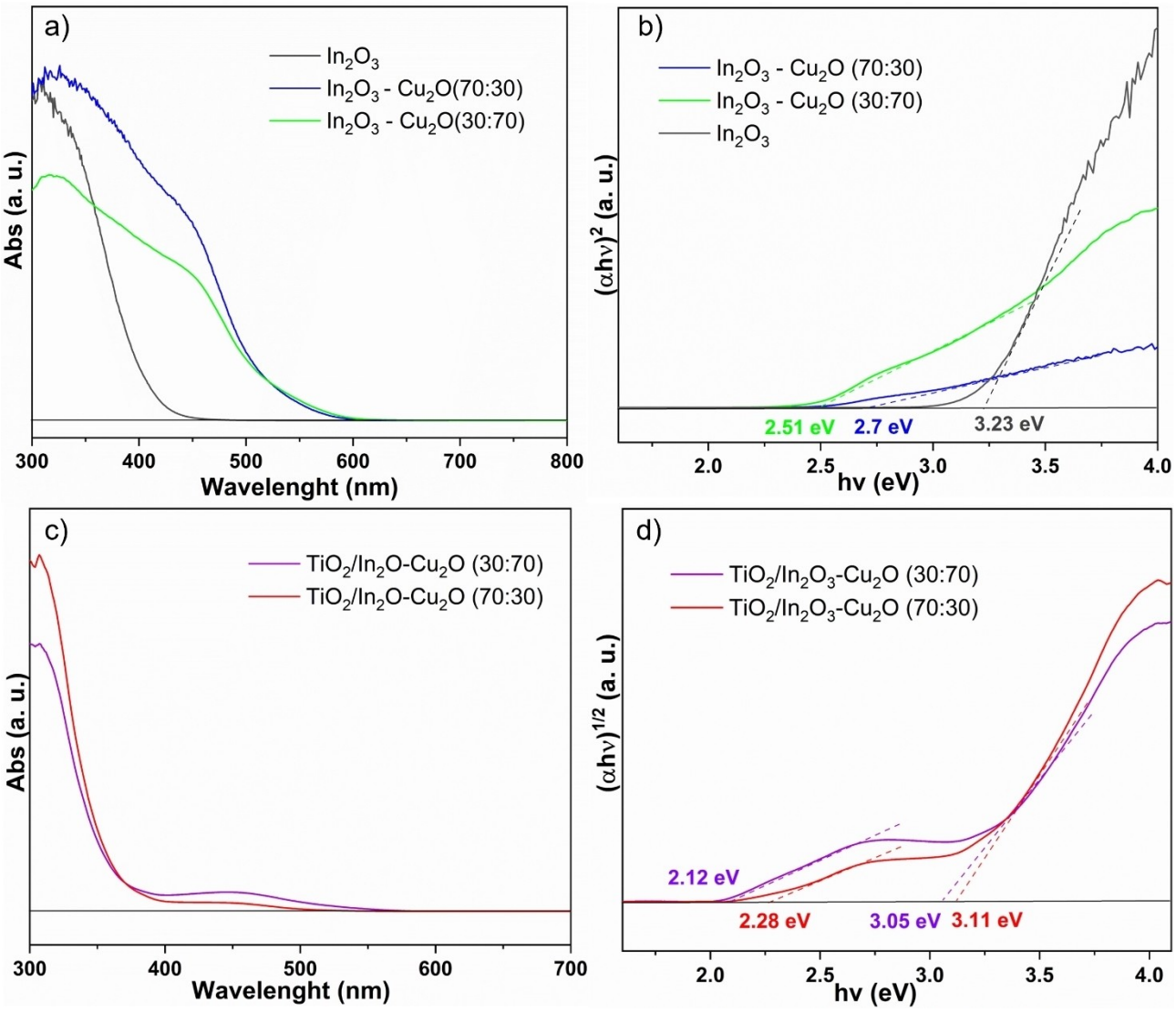

Figure 6. a) UV-Vis diffuse reflectance spectra of binary samples and b) corresponding Tauc plots; c) UV-Vis diffuse reflectance spectra of ternary samples TiO_2/In_2O_3-Cu_2O and d) corresponding Tauc plots.

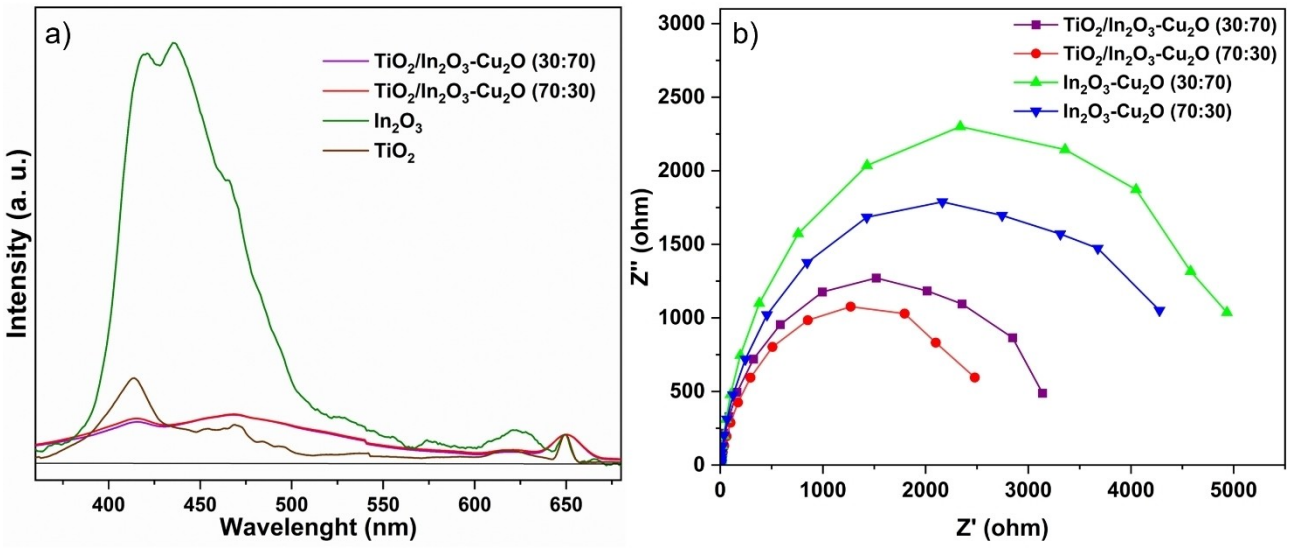

Figure 7. a) Comparison of photoluminescence spectra of pristine TiO_2, In_2O_3 and the ternary composites; b) Comparison of Nyquist plot of the binary In_2O_3-Cu_2O with different In:Cu ratio and of the ternary TiO_2/In_2O_3-Cu_2O.

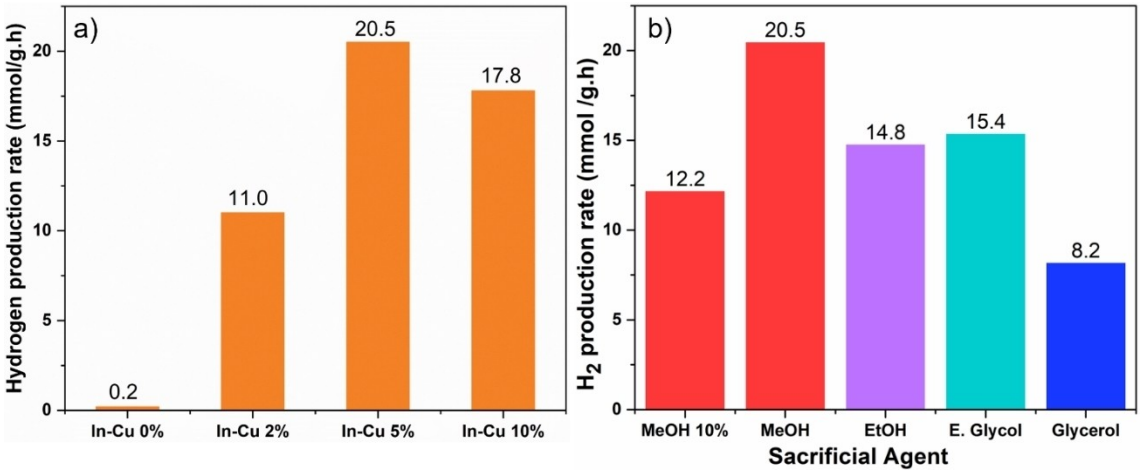

Figure 8. a) Comparison of TiO_2/In_2O_3-Cu_2O composites having variable amount of In_2O_3-Cu_2O (70:30), abbreviated as In–Cu; b) Comparison of different alcohols as sacrificial agents. The amount used was 20 vol % except the case of MeOH where also 10% was used. The label indicates the rate of hydrogen production in mmol/g h. Ethylen glycol is abbreviated as e. glycol.

detected at B.E. = 458.1 eV and B.E. = 463.8 eV assigned to Ti $2p_{3/2}$ and Ti $2p_{\frac{1}{2}}$ respectively,[46] going to the ternary composite, the peaks are shifted to higher binding energy ($\Delta = +0.5$ eV) resulting B.E. = 458.6 eV and B.E. = 464.3 eV meaning an electron depletion, meanwhile the spin-orbital splitting of +5.7 eV typical of Ti^{4+} is maintained unaltered in both samples. Concerning the core level XPS spectrum of Cu 2p, in the binary In_2O_3-Cu_2O (70:30) it was found Cu^+ as a largely predominant specie with the two typical components at B.E. = 932.4 eV and 952.1 eV attributed to Cu $2p_{3/2}$ and Cu $2p_{1/2}$ respectively (see Figure 5c). As a minor specie is present the oxide CuO as revealed by the peaks at B.E. = 934.4 eV and 953.8 eV and the shake–up peak in the region 940.5 – 948.5 eV which is diagnostic of the oxide.[47] Going to the ternary composite TiO_2/In_2O_3-Cu_2O, the amount of Cu(II) resulted increased at the expense of Cu(I) as clearly shown in Figure 5d.

Afterwards, to study the influence, if any, of the in situ growth of Cu_2O on In_2O_3 in the optical and electronic properties of the resulting binary and ternary composites, UV-Vis diffuse reflectance spectra were measured and are shown in Figure 6. Going from bare In_2O_3 to its binary composites with variable amount of Cu_2O, the absorbance shifts towards visible region as one could expect. Accordingly, the band gap energy is progressively reduced going from $E_g = 3.23$ eV for pure In_2O_3 to $E_g = 2.7$ eV for In_2O_3-Cu_2O (70:30) and 2.51 eV for In_2O_3-Cu_2O (30:70) as shown by the Tauc plot in Figure 6b, where both semiconductors have been considered as direct ones. Commercial TiO_2 nanoparticles have been used as host for the new cocatalyst In_2O_3-Cu_2O, their optical band gap was measured by UV-Vis DRS and resulted $E_g = 3.25$ eV as shown by the Tauc plot in Figure S14.

Afterwards, the optical properties of the corresponding ternary composites were studied and intriguingly, meanwhile they have very similar absorbance spectrum (see Figure 6c), two different band gap values can be derived for the nanocomposites having the co-catalyst In_2O_3-Cu_2O (70:30) and (30:70), see Figure 6d. Being TiO_2 the major component in 95 wt%, the ternary nanocomposites are approached as indirect semicond uctor and a band gap around 3.1 eV can be identified, as deriving from TiO_2, meanwhile the binary component In_2O_3-Cu_2O (70:30) or (30:70), gives rise to a narrower band gap, 2.28 and 2.12 eV respectively. Thus the loading of In_2O_3-Cu_2O on TiO_2 contributed to narrow significantly the bang gap and to shift the light absorbance to the visible region.

To study the migration and recombination of photo-generated charge carriers, photoluminescence (PL) spectroscopy was performed. As shown in Figure 7a, the PL curves of the two ternary composites are superimposable and have a peak at $\lambda = 413$ nm due to TiO_2 wherein the broad peak at around $\lambda = 467$ nm can be attributed to the In_2O_3 effect. Notably, the fluorescence emission intensity is dramatically diminished respect pristine TiO_2 and In_2O_3 indicating that the charge recombination in the new photocatalysts is largely quenched. Furthermore, electrochemical impedance spectroscopy (EIS) of the binary and ternary composites were measured. Expectedly, the arc radius of TiO_2/In_2O_3-Cu_2O was smaller respect to the binary compounds, see Figure 7b, indicating its surface is much more conductive to the migration of photo-generated electrons. Doing a comparison between the two ternary composites TiO_2/In_2O_3-Cu_2O, the one having In_2O_3-Cu_2O (70:30) shows minor resistance to charge transfer in agreement with its higher catalytic activity respect to In_2O_3-Cu_2O (30:70). Overall, these measurements confirm that a heterojunction structure was obtained by the *in situ* growth of Cu_2O NPs on In_2O_3 and further self-assembly with TiO_2 markedly enhances the transfer rate of photogenerated carriers and quenches the electron-hole recombination.

Photocatalytic Tests

We analyzed the solar-driven H_2 evolution process (HER) in deionized water using methanol as scavenger under simulated solar light irradiation. First of all, it was screened the effect on the reaction rate of the addition to TiO_2 of a variable amount (2.0, 5.0 and 10.0 wt%) of In_2O_3-Cu_2O (70:30) as co-catalyst. The corresponding ternary composites were tested and a volcano plot behavior was found as described in Figure 8a, where the best photocatalyst resulted the one containing 5 wt% of In_2O_3-Cu_2O, yielding 20.5 mmol/h.g, more than 100 times higher than pristine TiO_2. On these basis, a comparison among ternary photocatalysts where the co-catalyst In_2O_3-Cu_2O was modulated varying the In–Cu weight ratio as 70:30 and 30:70, was carried out. It was observed that under full spectrum of solar light, the best catalytic activity of 20.5 mmol H_2/h.g was reached again in the presence of TiO_2/In_2O_3-Cu_2O (70:30), using methanol as sacrificial electron donor (SED) as shown in Figure S11.

A screening of different sacrificial agents other than methanol was performed, by selecting a series of alcohols derived from the biomass as ethanol, ethylene glycol and glycerol. The best H_2 production rate i.e. 20.5 mmol/h.g could be reached in the presence of 20 vol % methanol (Figure 8b), and overwhelms the catalytic activity of similar TiO_2-based heterostructures as summarized in Table S2.

To prove the stability and recyclability of TiO_2/In_2O_3-Cu_2O, recycling tests were conducted, using the same conditions followed for the screening tests and after three run the H_2 production was maintained almost unaltered as shown by Figure S12. Electron microscopy inspection by SEM-EDAX showed for the recycled catalyst the same morphology and surface composition (see Figures S10c and S13b) of the fresh one, as outlined also by XRD comparison of fresh and recycled catalyst (Figure S13a).

We further studied the photo-induced electron-hole separation and charge kinetics that drives the photocatalytic reaction mechanism by evaluating the band edge potentials. The Mott-Schottky plots were analyzed to estimate the conduction band (CB) edge potentials. The flat band potential V_{fb} of pristine TiO_2, In_2O_3 and Cu_2O were −0.25 V, −0.48 V and −0.51 V vs. Ag/AgCl, respectively (see Figure 9a). Since the CB of the n-type semiconductor can be approximated as 0.1 V more negative than the V_{fb},[48] we added the calculated potentials vs. Ag/AgCl to the normal hydrogen electrode (NHE) scale using the equation $E_{NHE} = E_{Ag/AgCl} + 0.197$ and found that the corresponding CB potentials (E_{CB}) were −0.15 V (TiO_2), −0.38 V (In_2O_3) and −0.41 V (Cu_2O) respectively. Considering the optical band gap E_g previously measured for In_2O_3, TiO_2 and Cu_2O (see Figure 6 and Figure S14 respectively) being 3.23 eV, 3.25 eV and 2.65 eV respectively, the corresponding E_{VB} were evaluated according to the equation $E_{VB} = E_{CB} + E_g$ and resulted 3.11 V, 2.85 V and 2.25 V. On these basis, the energy level diagram could be derived (Figure 9b) where a type II heterojunction between p- and n-type semiconductors is established and it explains well the synergy among the three components and the resulting improved catalytic activity. DFT investigations are planned to provide a theoretical scheme of interaction and also further information on the photocatalytic mechanism.[49–50]

Examining carefully the Mott-Schottky plot (Figure 9a), it is evident a progressive negative shift of the V_{fb} going from pristine TiO_2, In_2O_3 and Cu_2O to the ternary nanocomposites TiO_2/In_2O_3-Cu_2O revealing an increase of carrier density N_D in the latter. Taking in consideration equation 1 reported below, that correlates N_D with the slope k of the linear portion of the Mott-Schottky graph:[51]

$$ND = \frac{2}{\varepsilon \cdot \varepsilon' \cdot e \cdot k} \quad (1)$$

where e, ε, ε′ are the elementary electron charge, dielectric constant and permittivity in vacuum respectively, it was calculated the N_D value in the two ternary nanocomposites and resulted 5.74×10^{-19} for TiO_2/In_2O_3-Cu_2O (70:30) and 3.87×10^{-19} for TiO_2/In_2O_3-Cu_2O (30:70), in agreement with the higher catalytic activity of the former.

Conclusions

By in situ growth of Cu_2O nanoparticles on In_2O_3 nanostructures and further assembly with TiO_2, a series of vis-light responsive photocatalysts were obtained with increased active sites and wider light absorption respect to pristine TiO_2 as testified by the narrower band gap. Comparing with bare In_2O_3 and TiO_2, a strong diminution of e^-/h^+ recombination and a significantly improved migration rate of photogenerated charge carriers was reached as evidenced by photoluminescence and Nyquist plot respectively. An highly extended interface contact between Cu_2O and In_2O_3 as arises from SEM and TEM, agrees withthe formation of a tight p-n heterojunction among the semiconductors which yields a greatly performing photocatalyst in the presence of different alcohols derived from the biomass. The best hydrogen production rate of 20.5 mmol/h g, was reached with methanol, overwhelming bare TiO_2 by 100 times. This opens the way to a further development and a wider application in photocatalysis of this class of nanomaterials, thanks also to the stability of the system and its easy scalability.

Acknowledgements

This research project has been partially funded by the European Union – NextGenerationEU under the Italian Ministry of University and Research (MUR) National Innovation Ecosystem grant ECS00000041 – VITALITY, CUP: B43C22000470005. M.C. thanks the project "FERMAT - Fast ElectRon dynamics in novel hybrid organic-2D MATerials" funded by the MUR Progetti di Ricerca di Rilevante Interesse Nazionale (PRIN) Bando 2017 - Grant number 2017KFY7XF for financing a post-doctoral grant to S. I. at CNR-ICCOM. The authors are grateful to Mr. Carlo Bartoli (CNR ICCOM) for the valuable technical assistance. Open Access publishing facilitated by Consiglio Nazionale delle Ricerche, as part of the Wiley - CRUI-CARE agreement.

Conflict of Interests

There are no conflicts to declare.

Data Availability Statement

The data that support the findings of this study are available from the corresponding author upon reasonable request.

Keywords: Cuprous oxide · Biomass · Hydrogen evolution · p-n heterojunction · Solar fuels

[1] M. Ikram, M. Rashid, A. Haider, S. Naz, J. Haider, A. Raza, M. T. Ansar, M. K. Uddin, N. M. Ali, S. S. Ahmed, M. Imran, S. Dilpazir, Q. Khan, M. Maqbool, *Sustainable Mater. Technol.* **2021**, *30*, e00343, https://doi.org/10.1016/j.susmat.2021.e00343.
[2] N. Goodarzi, Z. Ashrafi-Peyman, E. Khani, A. Z. Moshfegh, *Catalysts* **2023**, *13*, 1102, https://doi.org/10.3390/catal13071102.
[3] M. Sohail, S. Rauf, M. Irfan, A. Hayat, M. M. Alghmadi, A. A. El-Zahhrar, D. Ghernaout, Y. Al-Hadeethi, W. Lv, *Nanoscale Adv.* **2024**, *6*, 1286–1330.
[4] T. T. Le, P. Sharma, B. J. Bora, V. D. Tran, T. H. Truong, H. C. Le, P. Q. P. Nguyen, *Int. J. Hydrogen* **2024**, *54*, 791–816, https://doi.org.10.1016/j.ijhydene.2023.08.044.
[5] L. Zhang, C. Jia, F. Bai, W. Wang, S. An, K. Zhao, Z. Li, J. Li, H. Sun, *Fuel* **2024**, *355*, 129455, https://doi.org/10.1016/j.fuel.2023.129455.
[6] P. Hota, A. Das, D. K. Maiti, *Int. J. Hydrogen* **2023**, *48*, 523–541, https://doi.org/10.1016/j.ijhydene.2022.09.264.
[7] S. Nishioka, F. E. Osterloh, X. Wang, T. E. Mallouk, K. Maeda, *Nat. Rev. Methods Primers* **2023**, *3*, 42, https://doi.org/10.1038/s43586-023-00226-x.
[8] M. A. Deshmukh, S.-J. Park, H. N. Thorat, G. A. Bodkhe, A. Ramanavicius, S. Ramanavicius, M. D. Shirsat, T.-J. Ha, *J. Ind. Eng. Chem.* **2023**, *119*, 90–111, https://doi.org/10.1016/j.jiec.2022.11.054.
[9] E. Heo, S. Lee, H. Yoon, *Mater. Chem. Front.* **2023**, *7*, 6154–6187, https://doi.org/10.1039/D3QM00566F.
[10] L. C. Goveas, S. Nayak, R. Vinayagam, R. Selvaraj, A. Pugazhendhi, *Fuel* **2023**, *348*, 128460, https://doi.org/10.1016/j.fuel.2023.128460.
[11] M. Mohsin, T. Ishaq, I. A. Bhatti, Maryam, A. Jilani, A. A. Melaibari, N. H. Abu-Hamdeh, *Nanomaterials (Basel)* **2023**, *13*, 546, https://doi.org/10.3390/nano13030546.
[12] G. Di Liberto, L. A. Cipriano, S. Tosoni, G. Pacchioni, *Chem. – A Eur. J.* **2021**, *27*, 13306–13317, https://doi.org/10.1002/chem.202101764.
[13] C.-J. Sun, L.-P. Zhao, R. Wang, *Mini Rev. Org. Chem.* **2020**, *18*, 649–669, https://doi.org/10.2174/1570193x17999200820161301.
[14] X. Chen, S. S. Mao, *Chem. Rev.* **2007**, *107*, 2891–2959, https://doi.org/10.1021/cr0500535.
[15] B. Shang, L. Jiao, Q. Bao, C. Li, X. Cui, *Nano Mater. Sci.* **2019**, *1*, 231–245, https://doi.org/10.1016/j.nanoms.2019.09.002.
[16] D. Panchal, A. Sharma, S. Pal, *Mater. Today Sustainability* **2023**, *21*, 100264, https://doi.org/10.1016/j.mtsust.2022.100264.
[17] R. Ji, J. Liu, T. Zhang, Y. Peng, Y. Li, D. Chen, Q. Xu, J. Lu, *Sep. Purif. Technol.* **2021**, *272*, 118787, https://doi.org/10.1016/j.seppur.2021.118787.
[18] X. Zheng, Y. Song, Y. Liu, Y. Yang, D. Wu, Y. Yang, S. Feng, J. Li, W. Liu, Y. Shen, X. Tian, *Coord. Chem. Rev.* **2023**, *475*, 214898, https://doi.org/10.1016/j.ccr.2022.214898.
[19] D. Umaru, H. Y. Hafeez, J. Mohammed, A. B. Suleiman, C. E. Ndikilar, Y. Zakariyya, *Appl. Surf. Sci. Adv.* **2023**, *18*, 100520, https://doi.org/10.1016/j.apsadv.2023.100520.
[20] G. Zhou, Z. Zhou, Y. Xia, W. Yin, J. Hou, X. Zhu, J. Yi, S. Wang, X. Ning, X. Wang, *Appl. Surf. Sci.* **2023**, *608*, 154974, https://doi.org/j.apsusc.2022.154974.
[21] P. Chang, Y. Wang, Y. Wang, Y. Zhu, *Chem. Eng. J.* **2022**, *450*, 137804, https://doi.org/10.1016/j.cej.2022.137804.
[22] Kamlesh, D. Suthar, R. Sharma, G. Chasta, S. Panwar, Himanshu, L. P. Purohit, M. S. Dhaka, *Physica B* **2024**, *675*, 415622, https://doi.org/10.1016/j.physb.2023.415622.
[23] T. Kim, M. Chae, D. Lee, H. –D. Kim, *Opt. Mater.* **2024**, *149*, 115093, https://doi.org/10.1016/j.optmat.2024.115093.
[24] J. Zheng, W. Duan, Y. Guo, Z. C. Zhao, H. Yi, F. –J. Ma, L. G. Caro, C. Yi, J. Bing, S. Tang, J. Qu, K. C. Fong, X. Cui, Y. Zhu, L. Yang, A. Lambertz, M. A. Mahmud, H. Chen, C. Liao, G. Wang, M. Jankovec, C. Xu, A. Uddin, J. M. Cairney, S. Bremner, S. Huang, K. Ding, D. R. McKenzie, A. W. Y. Ho-Baillie, *Energy Environ. Sci.* **2023**, *16*, 1223–1233, https://doi.org/10.1039/D1EE04007G.
[25] M. Tahir, N. S. Amin, *App. Catal. B; Environ.* **2015**, *162*, 98–109, https://doi.org/10.1016/j.apcatb.201.06.037.
[26] Q. Du, J. Ma, X. Shao, W. Wang, G. Tian, *Chem. Phys. Lett.* **2019**, *714*, 28–212, https://doi.org/10.1016/j.cplett.2018.11.004.
[27] Z. M. Alaizeri, H. A. Alhadlaq, S. Aldawood, M. J. Akhtar, M. Ahamed, *Envir. Sci. Pollut. Res.* **2023**, *30*, 6055–6067, https://doi.org/10.1007/s11356-022-22594-9.
[28] X. Li, C. Fang, L. Huang, J. Yu, *J. Colloid Interface Sci.* **2024**, *655*, 485–492, https://doi.org/10.1016/j.jcis.2023.11.028.
[29] J. Liu, Y. Shang, X. Zou, S. Wu, Q. Zhong, *J. Colloid Interface Sci.* **2024**, *663*, 21–30, https://doi.org/10.1016/j.jcis.2024.01.172.
[30] Y. Li, X. Fang, Y. Liu, T. Zhang, Y. Zhao, Z. Guan, J. Wu, P. He, S. Yoriya, C. Zheng, L. Han, *Mater. Today Commun.* **2024**, *38*, 107997, https://doi.org/10.1016/j.mtcomm.2023.107997.
[31] Y. Tian, Y. Hong, B. Chen, K. Zhang, D. Hong, X. Lin, J. Shi, *Int. J. Hydrogen Energy* **2024**, *51*, 475–487, https://doi.org/10.1016/j.ijhydene.2023.08.223.

[32] N. Vinothkumar, M. De, *Int. J. Hydrogen Energy* **2014**, *39*, 11494–11500, https://doi.org/j.ijhydene.2014.05.095.
[33] X. W. Yang, H. L. Hou, Y. Yang, G. Z. Ma, X. Q. Zhan, H. L. Yang, W. Y. Yang, *Colloids Surf. A Physicochem Eng. Asp.* **2022**, *652*, 129881, https://doi.org/10.1016/j.colsurfa.2022.129891.
[34] S. Impemba, G. Provinciali, J. Filippi, C. Salvatici, E. Berretti, S. Caporali, M. Banchelli, M. Caporali, *Int. J. of Hydrogen Energy* **2024**, *63*, 896–904, https://doi.org/10.1016/j.ijhydene.2024.03.162.
[35] S. Rej, M. Bisetto, A. Naldoni, P. Fornasiero, *J. Mater. Chem. A* **2021**, *9*, 5915–5951, https://doi.org/10.1039/d0ta10181h.
[36] S. Sun, Q. Yang, S. Liang, Z. Yang, *Cryst. Eng. Comm* **2017**, *19*, 6225–6251, https://doi.org/10.1039/C7CE01530E.
[37] C. T. Rueden, J. Schindelin, M. C. Hiner, B. E. DeZonia, A. E. Walter, E. T. Arena, K. W. Eliceiri, *BMC Bioinform.* **2017**, *18*, 529, https://doi.org/10.1186/s12859-017-1934-z.
[38] D. Legland, I. Arganda-Carreras, P. Andrey, *Bioinformatics* **2016**, *32*, 3532–3534, https://doi.org/10.1093/bioinformatics/btw413.
[39] A. Casini, D. Chelazzi, R. Giorgi, *ACS Appl. Mater. Interfaces* **2021**, *13*, 37924–37936, https://doi.org/10.1021/ACSAMI.1C11064.
[40] G. Chinga, K. Syverud, *Nord. Pulp Pap. Res. J.* **2007**, *22*, 441–446, https://doi.org/10.3183/npprj-2007-22-04-p441-446.
[41] O. M. Berengue, A. D. Rodrigues, C. J. Dalmaschio, A. J. C. Lanfredi, E. R. Leite, A. J. Chiquito, *J. Phys. D: Appl. Phys.* **2010**, *43*, 045401, https://doi.org.10.1088/0022–3727/43/4/045401.
[42] D. V. Shinde, D. Y. Ahn, V. V. Jadhav, D. Y. Lee, N. K. Shrestha, J. K. Lee, H. Y. Lee, R. S. Mane, *J. Mater. Chem. A* **2014**, *2*, 5490, https://doi.org/10.1039/C3TA15407F.
[43] N. T. T. Mai, M. M. Neto, P. V. Thang, N. N. Trung, N. C. Tu, T. N. Dung, H. D. Chinh, L. T. L. Anh, *Mater. Trans.* **2020**, *61*, 1868, https://doi.org/10.2320/matertrans.MT-MN2019039.
[44] M. Rezaee, S. M. M. Khoie, K. H. Liu, *CrystEngComm.* **2011**, *13*, 5055, https://doi.org/10.1039/C1CE05185G.
[45] C. J. Howard, T. M. Sabine, F. Dickson, *Acta Crystallogr. Sec. B* **1991**, *47*, 462–468, https://doi.org/10.1107/S010876819100335X.
[46] N. Boonprakob, N. Wetchakun, S. Phanichphant, D. Waxler, P. Sherrell, A. Nattestad, J. Chen, B. Inceesungvorn, *J. Colloid Interface Sci.* **2014**, *417*, 402–409, https://doi.org/10.1016/j.jcis.2013.11.072.
[47] M. Wang, L. Sun, Z. Lin, J. Cai, K. Xie, C. Lin, *Energy Environ. Sci.* **2013**, *6*, 1211–1220, https://doi.org/10.1039/C3EE24162A.
[48] R. Lin, J. Wan, Y. Xiong, K. Wu, W.-C. Cheong, G. Zhou, D. Wang, Q. Peng, C. Chen, Y. Li, *J. Am. Chem. Soc.* **2018**, *140*, 9078–9082, https://doi.org/10.1021/jacs.8b05293.
[49] T. Liu, J. Huang, Z. Huang, Q. Luo, H. Wu, Y. Meng, C. He, H. Li, *Chem Eng. J.* **2024**, *486*, 150209.
[50] Z. Huang, J. Huang, T. Liu, Y. Wen, H. Wu, S. Yang, H. Li, *Chem. Eng. J.* **2024**, *485*, 149987.
[51] D. Ma, J.-W. Shi, Y. Zou, Z. Fan, J. Shi, L. Cheng, D. Sun, Z. Wang, C. Niu, *Nanoscale* **2018**, *10*, 7860–7870, https://doi.org/10.1039/C8NR00170G.

Manuscript received: August 6, 2024
Revised manuscript received: September 13, 2024
Accepted manuscript online: September 27, 2024
Version of record online: ■■, ■■

RESEARCH ARTICLE

Ternary nanocomposites have been developed by growing hierarchical Cu_2O nanospheres on In_2O_3 nanostructures and integrating them as a co-catalyst with TiO_2. In-depth microscopy analysis reveals Cu_2O is widespread on In_2O_3 with a highly extended contact surface. Photocatalytic tests show that Cu_2O-In_2O_3/TiO_2 systems enable a greatly increased H_2 production respect to bare TiO_2 using a variety of bio-alcohols as sacrificial agents.

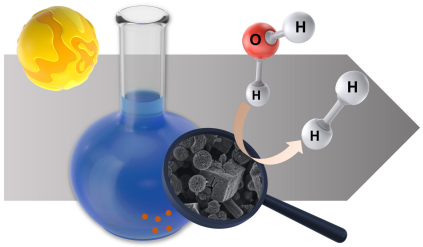

*S. Impemba, G. Provinciali, J. Filippi, S. Caporali, B. Muzzi, A. Casini, M. Caporali**

1 – 12

Tightly Interfaced Cu_2O with In_2O_3 to Promote Hydrogen Evolution in Presence of Biomass-Derived Alcohols